Development of a multi-scale ocean model by using particle Laplacian method for anisotropic mass transfer[‡]

Se-min Jeong[1], Toru Sato[2, *, †], Baixin Chen[3] and Shigeru Tabeta[1,2]

[1]*Department of Environment Systems, University of Tokyo, 5-1-5 Kashiwa-no-ha, Kashiwa 277-8563, Japan*
[2]*Department of Ocean Technology, Policy, and Environment, University of Tokyo, 5-1-5 Kashiwa-no-ha, Kashiwa 277-8563, Japan*
[3]*Department of Mechanical Engineering, Heriot-Watt University, Edinburgh EH14 4AS, U.K.*

SUMMARY

The direct injection of CO_2 into the deep ocean is one of the feasible ways for the mitigation of the global warming, although there is a concern about its environmental impact near the injection point. To minimize its biological impact, it is necessary to make CO_2 disperse as quickly as possible, and it is said that injection with a pipe towed by a moving ship is effective for this purpose. Because the injection ship moves over a spatial scale of $O(10^2\,km)$, a mesoscale model is necessary to analyse the dispersion of CO_2. At the same time, since it is important to investigate high CO_2 concentration near the injection point, a small-scale model is also required. Therefore, in this study, a numerical model was developed to analyse CO_2 dispersion in the deep ocean by using a fixed mesoscale and a moving small-scale grid systems, the latter of which is nested and moves in the former along the trajectory of the moving ship. To overcome the artificial diffusion of mass concentration at the interface of the two different grid systems and to keep its spatial accuracy almost the same as that in the small-scale, a particle Laplacian method was adopted and newly modified for anisotropic diffusion in the ocean. Copyright © 2010 John Wiley & Sons, Ltd.

1. INTRODUCTION

The Intergovernmental Panel on Climate Change published a special report on carbon capture and sequestration (CCS) and claimed that CCS may reduce CO_2 in the atmosphere [1]. The idea of CCS is that extremely large amount of CO_2 is sequestered in underground reservoirs or in the deep ocean. Among the CCS methods, ocean sequestration of CO_2 (COS) proposed by Marchetti [2] is considered to be effective because the amount of sequestered CO_2 in one selected site is comparatively larger than that of the geological storage. On the other hand, the main concern in the COS is its environmental impacts on marine organisms. In general, average current speed is believed to be small in the deep ocean, say $O(10^{-2}\,m/s)$, and we cannot expect quick dilution,

---

*Correspondence to: Toru Sato, Department of Ocean Technology, Policy, and Environment, University of Tokyo, 5-1-5 Kashiwa-no-ha, Kashiwa 277-8563, Japan.
†E-mail: sato-t@k.u-tokyo.ac.jp
‡This article was published online on [12 January 2010]. An error was subsequently identified. This notice is included in the online and print versions to indicate that both have been corrected [22 January 2010].

unlike that in the mixed layer. To diffuse the injected CO_2 effectively, a method to release liquid CO_2 from moving ships was suggested [3]. According to Nakashiki and Ohsumi [3], the total amount of the CO_2 sequestrated in one target site ($100\,km \times 100\,km$) is 10 million ton/year and a moving ship releases liquid CO_2 (LCO_2) droplets by injection pipes, the length of which is about 2000 m.

Within last decades, various numerical models were studied to predict the dilution process of CO_2 in various scales from $O(10^{-3}\,km)$ to $O(10^4\,km)$. Rising plume of CO_2 droplets released at the depths larger than 450 m was modelled by steady one-dimensional models [4, 5], where the plume consisting of CO_2 droplets and entrained water was treated as horizontal averages. To investigate the evolution and inner dynamics of two-fluid plumes, Thorkildsen and Alendal [6] simulated CO_2 droplet behaviour by solving a two-dimensional Navier–Stokes (NS) equation numerically. After that, unsteady, two-phase, three-dimensional (3D) models were developed [7–11] to predict the dilution process in the small scales ($O(10^{-3}\,km)$–$O(1\,km)$) around the injection point. These small-scale models predicted near-field distribution of physical and chemical properties, such as velocity, temperature, droplet volume fraction, CO_2 concentration, and pH. Meanwhile, the transfer of dissolved CO_2 concentration (DCO_2) dealt as passive dye in large scales ($O(10^4\,km)$) was simulated by a regional model of Masuda *et al.* [12].

The spatial scale of the COS system using the moving-ship method in an oceanic site is of $O(10^2\,km)$. On this scale, it is important to consider the trajectories of CO_2-releasing ships, because injected CO_2 may overlap the streaklines of CO_2 that was previously released. Although a large-scale regional model demonstrated to show the wide-range behaviour of DCO_2 and small-scale models were used to predict the dissolution from CO_2 droplets and the fate of DCO_2 near the injection points, models covering the spatial scale between them have not been developed so far except for a very recent work of Jeong *et al.* [13]. In [13], to resolve the distribution of DCO_2 in the mesoscale of $O(10^2\,km)$, a moving and nesting grid technique was developed: a small-scale domain is nested in a mesoscale domain and moves along the trajectory of a moving ship (Figure 1).

However, it needs careful attention when using such multiscale grid systems, because artificial diffusion occurs at their interface between the two grid systems due to the difference in grid size. When the small-scale domain, which represents the movement of a CO_2-releasing ship, moves back to its previous position and is faced with the seawater with previously discharged DCO_2, the DCO_2 re-entering the domain should have the same accuracy, i.e. spatial resolution, as that of the calculation done in the small-scale domain.

Therefore, the objective of this study is to greatly modify the multi-scale ocean model of Jeong *et al.* [13] to evaluate the overlap effect of the trajectory of the moving ship on DCO_2 without losing the resolution of the small-scale domain in the mesoscale domain. To achieve this, a Lagrangian particle method was considered and modified to adjust to the anisotropy of eddy diffusivity generally used in ocean physical models.
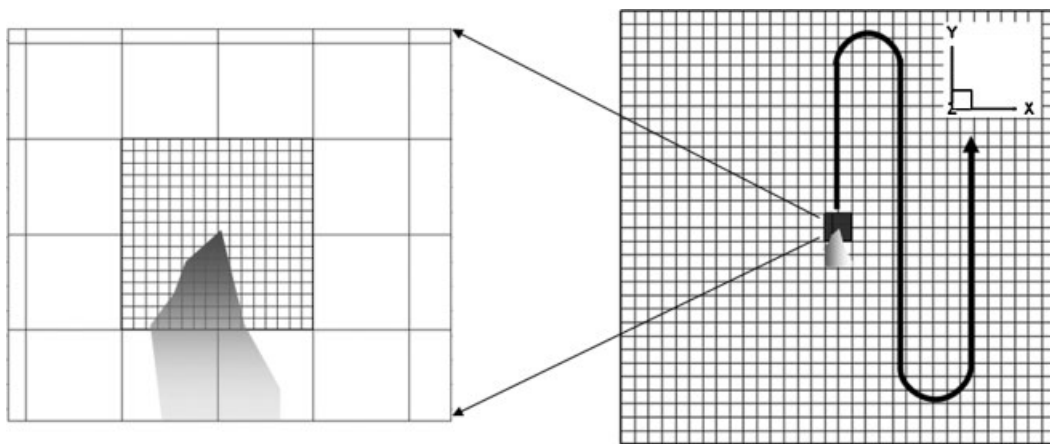

Figure 1. Schematic view of moving and nesting grid systems.

2. MATERIALS AND METHODS

2.1. Mesoscale model

The 30-s grid data of the Japan Hydrographic Association were collected and third-order spline was used to interpolate the topography for a candidate site from 131.4°E to 132.2°E and from 22°N to 23°N. The present grid system was rectangle on the horizontal plane and boundary-fitted curvilinear in the vertical direction. Assuming that surface water is almost separated from deep water by thermocline, the upper boundary of the computational domain was flat and set at the depth of 1000 m.

Difficulties lie in the determination of boundary conditions when open and deep oceanic fields are considered in numerical simulations. The present study adopted the low-wavenumber forcing technique of Sato *et al.* [14], by which energy cascades down from the large- to small-scale motions by the interactions of large–large, large–small, and small–small scales together with seabed topography, stratification, and rotation. Here, the large- and small-scales mean the scales larger and smaller than the computational domain, respectively.

The governing equations used in the mesoscale domain were the equation of continuity, the 3D, non-hydrostatic, Boussinesq-approximated NS equation including the Coriolis force, and the heat transfer equation:

$$\frac{\partial U_i^{\mathrm{H}}}{\partial x_i} = 0, \tag{1}$$

$$\frac{\partial U_i^{\mathrm{H}}}{\partial t} + \frac{\partial}{\partial x_j}\overline{\{(U_i^{\mathrm{L}}+U_i^{\mathrm{H}})(U_j^{\mathrm{L}}+U_j^{\mathrm{H}})\}} - f(U_2^{\mathrm{H}}\delta_{i1}+U_1^{\mathrm{H}}\delta_{i2})$$

$$= -\frac{1}{\rho_0}\frac{\partial P^{\mathrm{H}}}{\partial x_i} - \frac{\Delta\rho^{\mathrm{H}}}{\rho_0}\delta_{i3} + \frac{\partial}{\partial x_{j_H}}\left(\nu_{\mathrm{h}}\frac{\partial U_i^{\mathrm{H}}}{\partial x_{j_H}}\right) + \frac{\partial}{\partial x_3}\left(\nu_{\mathrm{v}}\frac{\partial U_i^{\mathrm{H}}}{\partial x_3}\right), \tag{2}$$

$$\frac{\partial T^{\mathrm{H}}}{\partial t} + \overline{(U_j^{\mathrm{L}}+U_j^{\mathrm{H}})\frac{\partial(T^{\mathrm{L}}+T^{\mathrm{H}})}{\partial x_j}} = \frac{\partial}{\partial x_{j_H}}\left(\kappa_{\mathrm{h}}\frac{\partial T^{\mathrm{H}}}{\partial x_{j_H}}\right) + \frac{\partial}{\partial x_3}\left(\kappa_{\mathrm{v}}\frac{\partial T^{\mathrm{H}}}{\partial x_3}\right), \tag{3}$$

where U_i, P, and T are the velocity components, the pressure, and the temperature, respectively, in the mesoscale domain, f is the Coriolis parameter, ρ_0 is the reference density of seawater, g is the gravitational acceleration, and ν_{h}, ν_{v}, κ_{h}, and κ_{v} are the horizontal and vertical eddy viscosities and diffusivities, respectively. The subscript, j_H, for the coordinates indicates the horizontal directions: i.e. $j_H = 1$ and 2. The superscripts, L and H, for the velocity and the temperature are the low- and high-wavenumber components. The overbars in Equations (2) and (3) indicate a domain-scale high-pass filter to remove low-wavenumber components generated inside the computational domain. The reason why the generated waves larger than the domain scale were removed is that all the low-wavenumbers should be given as forcing components, which already include the generated cascade-ups.

The low-wavenumber components in the convection terms (U_i^L and T^L) in Equations (2) and (3) are forcing terms. For the mesoscale model, the low-wavenumbers were given by the spectral analysis of measured transient data and used together with a realistic topography. The vertical velocity component was not forced because it is far smaller than the other components, particularly in the low-wavenumber regime.

The Richardson's power law was used for the horizontal eddy viscosities and diffusivities:

$$\nu_{\mathrm{h}} = \kappa_{\mathrm{h}} = \gamma\Delta^{1.15}, \tag{4}$$

where the scaling coefficient γ was set to be 0.000206, Δ is the grid scale in m, and the exponent is after Okubo [15]. Δ in the mesoscale domain is 3481 m, as will be described later in Section 3.1. Hence, the viscosity is 2.44 m^2/s, which is reasonable compared with measurements (e.g. [16]).

For the vertical eddy viscosities and diffusivities, the stratification function model [17] was adopted:

$$v_v = v_{v0}(1 + \beta Ri)^\alpha, \tag{5}$$

$$\kappa_v = \kappa_{v0}(1 + \beta Ri)^\alpha, \tag{6}$$

where $Ri = -(g(\partial\rho/\partial z))/(\rho_0(\partial u/\partial z)^2)$ is the Richardson number and v_{v0} and κ_{v0} are the reference eddy viscosity and diffusivity, respectively. α and β in Equations (5) and (6) were set to be -1.0, 5.2, and -0.5, 3.3, respectively, following Munk and Anderson [18].

Boundary conditions are necessary only for the high-wavenumber components and were set to be periodical in the horizontal directions. In the vertical direction, top and bottom boundaries adopted free-slip condition. This was not only because the grid resolution necessary for the turbulent boundary layer is expensive in computation, but also because it is believed that the effect of the Ekman layer does not reach the middle layer that is the centre of our interest and the generation of internal waves associated with the topography can be regarded as inviscid behaviour.

The Marker-and-Cell-type algorithm was applied to formulate the finite volume method (FVM) of the above governing equations. For the spatial differentiation of the convection term of the NS and heat transfer equations, a third-order upwinding scheme was adopted. The other terms had the second-order accuracy. The second-order Adams–Bashforth method was used for the time integration of the NS equation.

Proceeding to the main calculation, an oceanic flow field was simulated only in the mesoscale domain using the low-wavenumber forcing. An instantaneous velocity vector field and a wavenumber energy spectrum 30 days after the start of the forcing are depicted in Figure 2(a) and (b), respectively. In Figure 2(b), the curve and vertical bars denote the generated high-wavenumber and the forcing low-wavenumber components, respectively. It is found that energy cascades down from forced low wavenumbers to generated high wavenumbers smoothly. The comparison between the measurement and the calculation in temporal change of velocity components and frequency-based energy spectra shown in Figure 2(c) and (d), respectively, agree moderately well. This may evidence the validity of the adopted low-wavenumber forcing.

2.2. Small-scale model

To generate fluctuations in the small-scale domain, the low-wavenumber forcing was also used. This time, the forcing low-wavenumber components of velocity and temperature for the small-scale domain contain the high-wavenumber components for the mesoscale domain: i.e. the waves larger than the small-scale domain within the high-wavenumbers generated in the mesoscale domain were also used as forcing components, together with those used in the mesoscale domain.

The governing equations for the small-scale domain are

$$\frac{\partial u_i^H}{\partial x_i} = 0, \tag{7}$$

$$\frac{\partial u_i^H}{\partial t} + \frac{\partial}{\partial x_j}\overline{\{(u_i^L + u_i^H - u_i^{SHIP})(u_j^L + u_j^H - u_j^{SHIP})\}} - f(u_2^H \delta_{i1} + u_1^H \delta_{i2})$$

$$= -\frac{1}{\rho_0}\frac{\partial p^H}{\partial x_i} - \frac{\Delta\rho^H}{\rho_0}\delta_{i3} + \frac{\partial}{\partial x_{j_H}}\left(v_h\frac{\partial u_i^H}{\partial x_{j_H}}\right) + \frac{\partial}{\partial x_3}\left(v_v\frac{\partial u_i^H}{\partial x_3}\right), \tag{8}$$

$$\frac{\partial \tau^H}{\partial t} + \overline{(u_j^L + u_j^H - u_j^{SHIP})\frac{\partial(\tau^L + \tau^H)}{\partial x_j}} = \frac{\partial}{\partial x_{j_H}}\left(\kappa_h\frac{\partial \tau^H}{\partial x_{j_H}}\right) + \frac{\partial}{\partial x_3}\left(\kappa_v\frac{\partial \tau^H}{\partial x_3}\right), \tag{9}$$
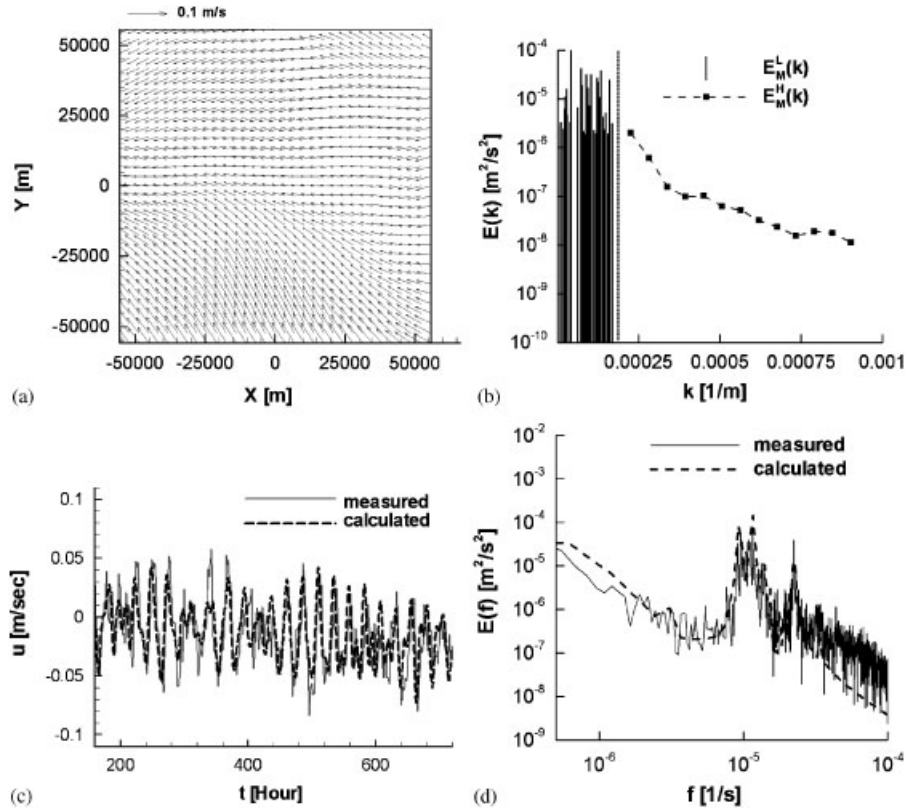
Figure 2. Instantaneous velocity vector field (a) and wavenumber energy spectrum (b) 30 days after the start of CO_2 injection at $z=-2000\,m$, and temporal change of velocities (c) and frequency energy spectrum (d) at the centre of the domain. In (b), vertical bars are forcing components and a line with closed squares indicates generated high-wavenumber components.

where

$$u_i^L = U_i^L + \hat{U}_i^H, \tag{10}$$

$$\tau^L = T^L + \hat{T}^H, \tag{11}$$

and u_i, p, and τ are the velocity components, the pressure, and the temperature, respectively, in the small-scale domain. u_j^{SHIP} is the ship velocity, which was introduced by the arbitrary Lagrangian–Eulerian method to move the small-scale grid system in the mesoscale domain. The hat ˆ in Equations (10) and (11) indicates the low-pass filter to exclude the waves shorter than the size of the small-scale domain.

Boundary conditions for the high-wavenumber components were set to be periodical in all the directions.

2.3. Particle anisotropic Laplacian method for DCO_2 diffusion

In particle Laplacian-based methods, such as the smoothed particle hydrodynamics method [19] for compressible fluids in the astrophysical problem and the moving particle semi-implicit method (MPS) [20] for the application to the incompressible fluids, the advection of a physical property is presented by the Lagrangian movements of particles and its diffusion is solved by the interactions of neighbour particles by using a Laplacian operator. The Laplacian operator of the MPS for any

variable ϕ is modelled by

$$\langle \nabla^2 \phi \rangle_m = \frac{2d}{N_m \lambda_m} \sum_{n \neq m} [(\phi_n - \phi_m) w(|\mathbf{r}_n - \mathbf{r}_m|)], \tag{12}$$

$$w(r) = \begin{cases} \dfrac{r_e}{r} - 1, & (0 \leqslant r \leqslant r_e) \\ 0, & (r_e \leqslant r) \end{cases}, \tag{13}$$

$$N_m = \sum_{n \neq m} [w(|\mathbf{r}_n - \mathbf{r}_m|)], \tag{14}$$

$$\lambda_m = \frac{\int w(r) r^2 \, dv}{\int w(r) \, dv} \approx \frac{1}{N_m} \sum_{n \neq m} [w(|\mathbf{r}_n - \mathbf{r}_m|) |\mathbf{r}_n - \mathbf{r}_m|^2]. \tag{15}$$

where $w(r)$ is the weighting function, r_e is the effective radius, d is the coefficient for the dimension, e.g. 3 for a 3D problem, N_m is the particle density at a coordinate r_m, and λ_m is a coefficient for adjusting the variance of the distribution in the analytical solution. The effective radius is defined by the production of a coefficient and an initial distance between a pair of particles, and the coefficient varied in the range from 1.5 to 4.1, according to Koshizuka and Oka [20].

When DCO_2 exits from the small-scale domain to the mesoscale domain, particles representing DCO_2 are released. In this study, the particles were moved by velocities that were interpolated trilinearly from the mesoscale Eulerian FVM calculation to reduce the computational time, and only the diffusion of DCO_2 was analysed by using the particle Laplacian operator. The mass transfer equation in the ocean is given by:

$$\frac{DC}{Dt} = \kappa_h \left[\frac{\partial^2 C}{\partial x^2} + \frac{\partial^2 C}{\partial y^2} \right] + \kappa_v \frac{\partial^2 C}{\partial z^2}. \tag{16}$$

The diffusivity in the vertical direction is highly different from that in the horizontal direction in ocean models: e.g. κ_v is 10^3–10^6 times smaller than κ_h in general. Because of this anisotropic character, it is necessary to modify the original Laplacian operator of the MPS. We considered a transformed coordinate system (x, y, and ζ) for the mass transfer equation in the present ocean model:

$$\frac{DC}{Dt} = \kappa_h \left[\frac{\partial^2 C}{\partial x^2} + \frac{\partial^2 C}{\partial y^2} + \frac{\partial^2 C}{\partial \zeta^2} \right], \tag{17}$$

where

$$\frac{\partial \zeta}{\partial z} = \sqrt{\frac{\kappa_h}{\kappa_v}}. \tag{18}$$

where κ_h is calculated by Equation (4) with a constant Δ, which is the horizontal grid size, not the temporally changing particle distance.

The sphere in the transformed (x, y, and ζ) coordinates is now a spheroid in the Cartesian (x, y, and z) coordinates, as are shown by solid lines in Figure 3. Because it is necessary to keep $\partial \zeta / \partial z$ constant, the vertical diffusion coefficient defined by Equation (6) was calculated using the Richardson number based on the initial field and is kept constant with time during the calculation.

Since the weighting function in the Laplacian operator is the function of the distance from a particle to the others, modification based on the distance in the transformed domain is derived
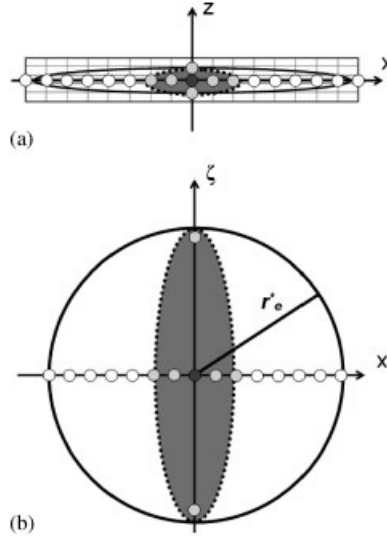
Figure 3. Ranges for searching neighbour particles in the Cartesian (a) and transformed (b) domains. Solid and dashed lines denote optimal and realistic ranges, the former of which is a sphere in the transformed domain.

from the above relation:

$$\langle \nabla^2 \phi \rangle_m^* = \frac{2d}{N_m^* \lambda_m^*} \sum_{n \neq m} [(\phi_n - \phi_m) w(|\mathbf{r}_n^* - \mathbf{r}_m^*|)], \tag{19}$$

$$r^* = |\mathbf{r}_n^* - \mathbf{r}_m^*| = \sqrt{(x_n - x_m)^2 + (y_n - y_m)^2 + \frac{\kappa_h}{\kappa_v}(z_n - z_m)^2}, \tag{20}$$

$$w(r^*) = \begin{cases} \dfrac{r_e^*}{r^*} - 1 & (0 \leqslant r^* \leqslant r_e^*) \\ 0 & (r_e^* \leqslant r^*) \end{cases}, \tag{21}$$

$$N_m^* = \sum_{n \neq m} [w(|\mathbf{r}_n^* - \mathbf{r}_m^*|)], \tag{22}$$

$$\lambda_m^* = \frac{1}{N_m} \sum_{n \neq m} [w(|\mathbf{r}_n^* - \mathbf{r}_m^*|)|\mathbf{r}_n^* - \mathbf{r}_m^*|^2]. \tag{23}$$

Finally, the mass-transfer equation becomes:

$$\frac{DC}{Dt}\bigg|_m = \kappa_h \left[\frac{\partial^2 C}{\partial x^2} + \frac{\partial^2 C}{\partial y^2} + \frac{\partial^2 C}{\partial \zeta^2}\right]_m = \kappa_h \frac{2d}{N_m^* \lambda_m^*} \sum_{n \neq m} [(C_n - C_m) w(|\mathbf{r}_n^* - \mathbf{r}_m^*|)]. \tag{24}$$

Hereafter, we call the present particle method for anisotropic diffusivity as the particle anisotropic Laplacian method (PAIL).

The objective of the use of the PAIL is to keep the resolution of DCO_2 in the mesoscale domain being almost the same as that in the Eulerian FVM calculation in the small-scale domain. In this context, the particles, which are released at the interface between the small-scale and the mesoscale domains, should be placed at the intervals almost equivalent to the grid sizes of the small-scale domain. However, this makes particle density uneven in the horizontal and vertical directions in the transformed coordinates, as shown in Figure 3(b). For instance, $dx = dy = 435.2\,\mathrm{m}$ and $d\zeta = 4941.1\,\mathrm{m}$ when $dz = 156.3\,\mathrm{m}$ and $\partial \zeta/\partial z = 1000$. The number of particles in the horizontal directions becomes too many in a spherical particle-search range, and too many particles in the

Laplacian operator results in too much computational time and memory. To cope with this, a vertically long spheroid, which is drawn by a dashed line in Figure 3(b), was considered in the transformed coordinates when searching neighbour particles. This means that priority is given to the uniformity of the particle density more than the shape of the particle-search range in the transformed coordinates in this study. In the Cartesian coordinates, the corresponding spheroid has the long horizontal principal axis, as is also shown by a dashed line in Figure 3(a).

At any boundary of the small-scale domain, particles were released if DCO_2 is larger than 0.10 ppm at every time step of the mesoscale calculation. At the time, neighbour particles were also placed around these DCO_2-representing particles to calculate the diffusion of DCO_2 by the PAIL, as shown in Figure 4. The initial DCO_2 held by these particles was calculated by a trilinear interpolation of FVM values in the small-scale domain.

When the small-scale domain moved and the particles drifted in the mesoscale domain re-enter the small-scale domain, DCO_2 held by the particles were transferred to the cell-wise values in the small-scale domain by treating it as a convection flux

$$\frac{1}{V}\int \frac{\partial(u_j C)}{\partial x_j}\mathrm{d}V = \frac{1}{V}\oint C\mathbf{u}\cdot\mathrm{d}\mathbf{S} = \frac{1}{V}\left(\sum_{k=1}^{5} C\mathbf{u}\cdot\mathrm{d}\mathbf{S}_k + \frac{1}{m_{\mathrm{tot}}}\sum_{m=1}^{m_{\mathrm{tot}}} C_m\mathbf{u}^{\mathrm{SHIP}}\cdot\mathrm{d}\mathbf{S}_{\mathrm{front}}\right), \qquad (25)$$

where V is the volume of a small-domain cell that swallows particles, k is the cell-face number other than the front face, m and m_{tot} are the index and the total numbers of particles entering the cell, respectively. This process is shown schematically in Figure 5. After transferred to the cell-wise DCO_2, the particles swallowed by the cell were not used in the PAIL anymore and, hence, removed.
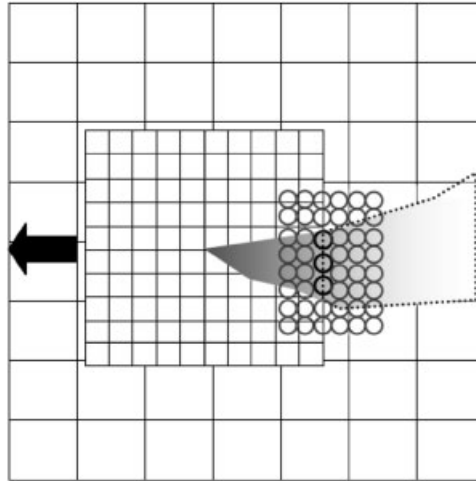

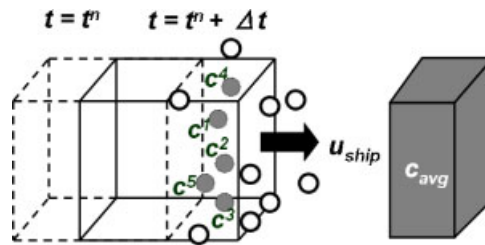Figure 4. Schematic view of particles release at the exit of small-scale domain.

Figure 5. Schematic view of flux treatment of re-entering particles into small-scale domain.

In this study, time increments, Δt, were constant, set to be 43.5 and 174.0 s in the small-scale and the mesoscale domains, respectively. The particles swallowed by the small-scale domain were originally released from the domain at every time step of the mesoscale calculation, i.e. every 174.0 s. Therefore, the number of particles entering a cell in the small-scale domain was sometimes less than 1 in each time increment of the small-scale calculation, 43.5 s. This may make DCO_2 in the small-scale domain brindle. To avoid this, zero-gradient Neumann boundary condition was applied when the number of the entering particles was zero at the front boundary of the small-scale domain.

To find the optimum coefficients for effective radius, preliminary calculations were carried out. The sizes of the computational domain and grids are the same as those of the small-scale domain used in the following ocean calculation: $Lx = Ly = 6693$ m and $Lz = 850$ m and $dx = dy = 435.2$ m and $dz = 156.3$ m, respectively. Initial mass concentration was $C_0 = 100$ and placed in a hexahedron, the size of which was 0.2 times of the domain size, at the centre. The spatial intervals between the particles were the same as the grid size. The ratio of the diffusivities in the horizontal and the vertical directions was set to be 1000. The total calculation time was 10^7 s. In this calibration, the mass diffusion only in the small-scale domain was considered and there were no flows and the domain did not move.

The results of the calculations are illustrated in Figure 6, where the colours of the particles and contours denote the mass concentration in Cases A1, A2, and B1. If the PAIL and the FVM ideally give the same results, the colours at the same position should be the same. The errors between them are summarized in Table I, where R_x, R_y, and R_z are the coefficients for the effective radius in the x, y, and z directions, respectively. The averaged and the maximum errors were calculated by

$$\text{Error}_{\text{avg}} = \frac{1}{C_0} \sqrt{\frac{1}{n} \sum (C_{\text{EUL}} - C_{\text{PAIL}})^2}, \tag{26}$$

$$\text{Error}_{\text{max}} = \frac{1}{C_0} |C_{\text{EUL}} - C_{\text{PAIL}}|_{\text{max}}, \tag{27}$$

where C_{EUL} and C_{PAIL} are the mass concentrations calculated by the Eulerian FVM and the PAIL, respectively. Although the errors slightly increased when the particles were randomly distributed, they were still small and the coefficients in Case A1 were used in the following ocean calculations. This test calculation gave not only the optimum parameters but also the validation of the PAIL.

3. RESULTS AND DISCUSSION

3.1. Simulation conditions

By using the above-mentioned methods, CO_2 diffusion was simulated for the COS using a moving ship. DCO_2 was treated as passive dye and the advection–diffusion equation was solved by the FVM in the small-scale domain. When DCO_2 exited from the small-scale domain to the mesoscale domain, particles were released at the outlet and their advection and diffusion were solved by the PAIL. The operation area of the CO_2 releasing ship and the way how the ship moves are illustrated in Figure 7. The small-scale domain moves at the speed of 2.5 m/s along the trajectory with the CO_2 injection rate of 100 kg/s. The injection depth was set to be 2000 m. This corresponds to the COS of 10 million ton per year in a 100 km^2 oceanic domain.

Figure 8 shows the grid systems for this simulation. The dimensions of the mesoscale and the small-scale domains were $111.4 \times 111.4 \times 5.1$ km and $6693 \times 6693 \times 850$ m in the x, y, and z directions, respectively. The numbers of grids were $32 \times 32 \times 31$ and $16 \times 16 \times 5$ in the mesoscale and the small-scale domains, respectively. Therefore, the size of the small-scale domain matches 2×2 cells of the mesoscale domain in the horizontal plane and vertical layers exactly match those of the mesoscale domain. This means that the minimum wavelength in the mesoscale domain was the same as the maximum wavelength in the small-scale domain and, eventually, all the waves generated in the mesoscale domain were used in the small-scale domain as forcing components
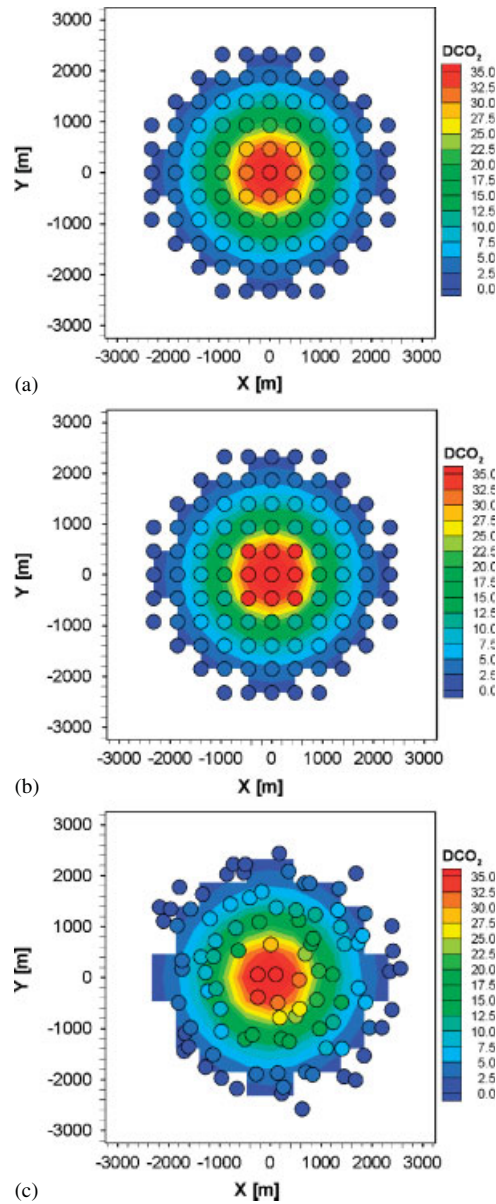
Figure 6. Contour maps of DCO_2 in particles and grids in small-scale domain in
Cases: (a) A1; (b) A2; and (c) B1.

$(\hat{U}_i^H = U_i^H)$. Therefore, the low-pass filter in Equation (10) was not operated in the present study
and, instead, the nondimensional threshold wavenumbers of the high-pass filters in Equations (8)
and (9) were both 1 based on the size of the small-scale domain, where the nondimensional
wavelength of 1 was excluded by the filter.

3.2. Results and discussion

In Figure 9, the energy spectrum in the small-scale domain is depicted 30 days after the start of
CO_2 injection. A curve connecting closed squares and vertical bars denotes the generated high
wavenumbers and the forced low wavenumbers, respectively. The generated high wavenumbers
and the forced low wavenumbers in the mesoscale domain were used as forcing components in the
small-scale domain. It can be found that energy cascades down to high wavenumbers properly.

Table I. Average and maximum errors between FVM and PAIL.

Case	R_x	R_y	R_z	Particle distribution	Error (avg.)	Error (max.)
A1	2.1	2.1	1.1	Regular	1.4940×10^{-2}	5.3586×10^{-2}
A2	4.1	4.1	1.1	Regular	4.4286×10^{-2}	11.7028×10^{-2}
B1	2.1	2.1	1.1	Random	2.4827×10^{-2}	7.7167×10^{-2}
B2	4.1	4.1	1.1	Random	4.9359×10^{-2}	16.9352×10^{-2}
A3	2.1	2.1	1.01	Regular	2.2637×10^{-2}	8.3036×10^{-2}
B3	2.1	2.1	1.01	Random	3.1209×10^{-2}	7.5292×10^{-2}
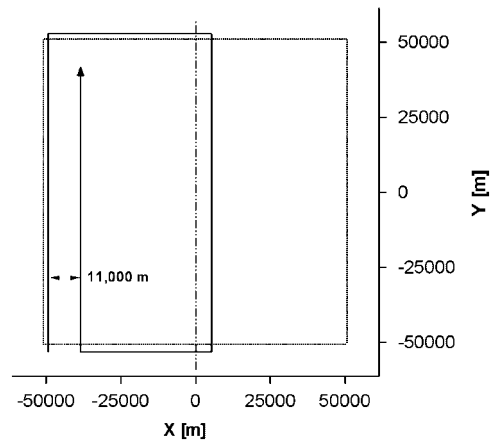
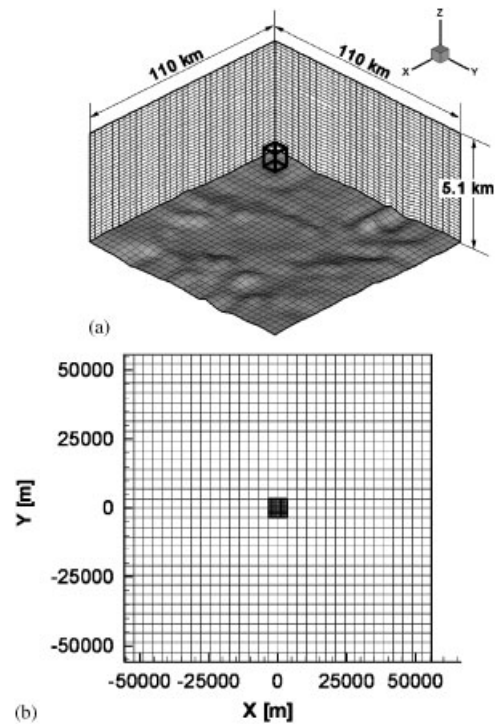Figure 7. Schematic views of operation area in the ocean and trajectory of a moving ship.

Figure 8. Computational grid systems for meso and small-scale domains.
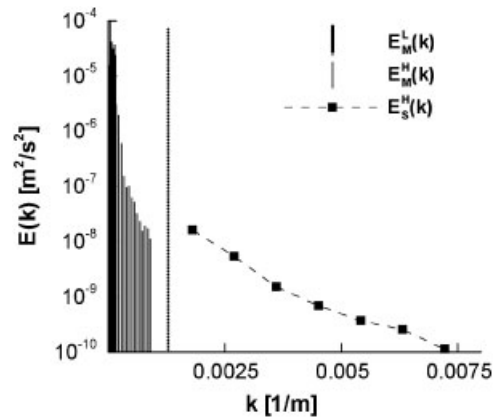
Figure 9. Wavenumber energy spectrum in the small-scale domain on the plane at $z = -2000\,m$ 30 days after the start of CO_2 injection. Vertical bars in low-wavenumber range are forcing components, which are the forcing and generated components in the mesoscale domain, and a line indicates generated high-wavenumber components in the small-scale domain.
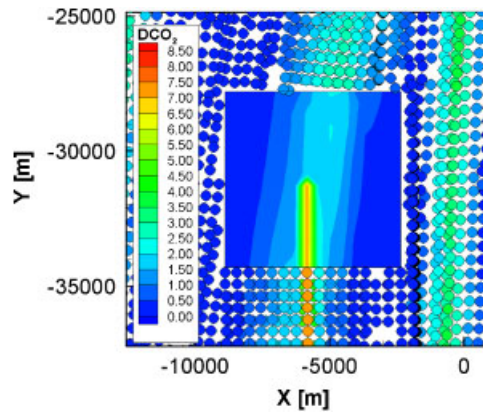

Figure 10. Particles released to the wake direction and swallowed at the front face of small-scale domain on the plane at $z = -2000\,m$. The colours of the particle and those in the small-scale grids indicate DCO_2 in the same range.

Figure 10 shows that particles were released in the wake of the moving domain and re-entering particles were swallowed at the front interface of the domain on a horizontal plane. The colours of the particles and those filled in the small-scale domain grids represent DCO_2 calculated by the PAIL and the FVM, respectively. It should be noted that the illustrated particles were not exactly on the flat plane but existed within $\pm 5\,m$ from the plane. It seems that the treatment of particles at the interface worked well because DCO_2 of the released and the re-entering particles were reasonably continuous to those calculated by the FVM.

The contour maps of DCO_2 14 and 21 days after the start of CO_2 injection are shown in Figure 11. The streaklines of released DCO_2 overlapped each other and were dispersed by tidal currents and eddy diffusivity.

Figure 12 shows the histograms of water volume against the increase of PCO_2 (ΔPCO_2) in the meso and the small-scale domains. ΔPCO_2 was calculated by subtracting PCO_2 based on the background DCO_2 from that of total DCO_2. It is possible to use these histograms to evaluate the environmental effects caused by the COS, together with measured impacts of PCO_2 on deep-sea organisms in the future.
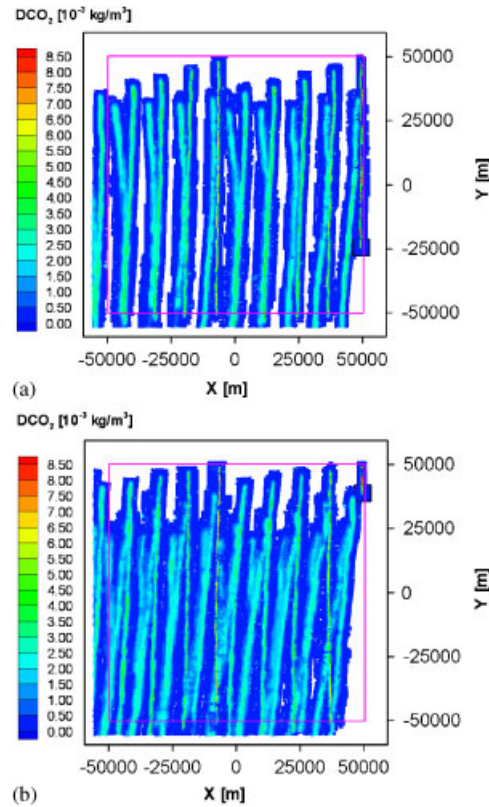
Figure 11. Contour maps of DCO_2 14 (a) and 21 (b) days after the start of CO_2 injection on the plane at $z = -2000\,m$.

Recent researches, such as Kikkawa *et al.* [21], elucidated that the biological impacts of CO_2 in the ocean should not be related only to pH but also to PCO_2, because the same low pH caused by CO_2 as that by some strong acid agents, such as hydrochloric and sulphuric acids, results in more damages on marine organisms than the cases by the above acids. For the calculation of PCO_2, a code developed by Carbon Dioxide Information Analysis Center (CDIAC, http://cdiac.ornl.gov/oceans/co2rprt.html) was used with the coefficients of Roy *et al.* [22]. For the quantitative estimation of the biological impact of ΔPCO_2 in the deep ocean, criteria were proposed by Kita and Watanabe [23]: i.e. the no-observed effect concentration for various organisms and the predicted no-effect concentration are 5000 and 500 μ atm, respectively. Although these values have not been authorized, we can refer them as tentative standards and, in Figure 12, it is clear that there are little water with ΔPCO_2 of more than 500 μ atm both in the meso and small-scale domains.

4. CONCLUSION

To predict the dispersion behaviour of DCO_2 injected in the deep ocean, a multi-scale ocean model was developed: a small-scale domain (O(1 km)) with fine resolution was nested in the mesoscale domain (O(10^2 km)) and moved along the trajectory of a ship, which tows a CO_2-injection pipe. To prevent the artificial diffusion of mass concentration at the interface of the two different grid systems, the PAIL was newly developed, where the original particle method was modified for the anisotropic diffusion in the ocean. It is also thought that the developed method has large applicability to other multi-scale mass transfer problems in the ocean.
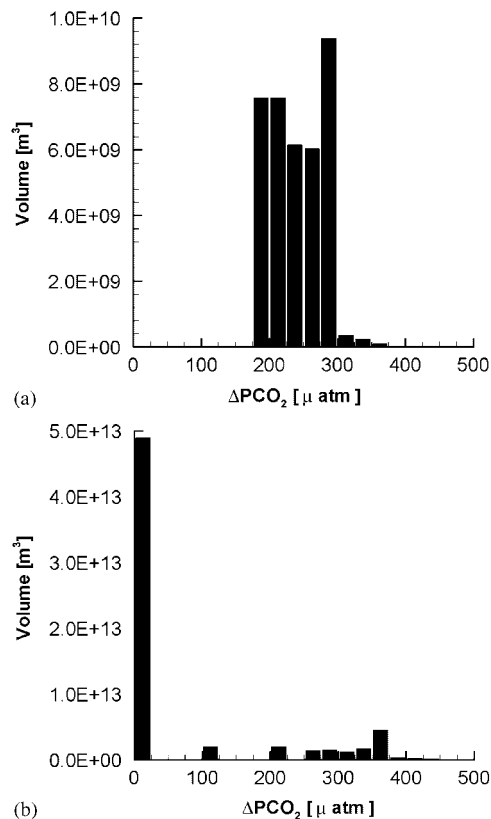
Figure 12. Histograms of water volume against ΔPCO_2 21 days after the start of CO_2 injection in small-scale (a) and mesoscale (b) domains.

The results of CO_2 diffusion simulation imply that the developed model is applicable to estimate environmental impacts together with experimental data of marine biota. Moreover, the model can also be useful for optimizing the trajectory of the releasing ship, the depths of CO_2 injection, and the flow rate of CO_2 at each depth to minimize the biological impacts of CO_2. They are left for our future study.

REFERENCES

1. Intergovernmental Panel on Climate Change (IPCC). *IPCC Special Report on Carbon Dioxide Capture and Storage*, 2005.
2. Marchetti C. On geoengineering and the CO_2 problem. *Climatic Change* 1997; **1**:59–68.
3. Nakashiki N, Ohsumi T. Dispersion of CO_2 injected into the ocean at the intermediate depth. *Energy Conversion and Management* 1997; **38**:355–360.
4. Liro CR, Adams EE, Herzog HJ. Modeling the release of CO_2 in the deep ocean. *Energy Conversion and Management* 1992; **33**:667–674.
5. Drange H, Alendal G, Haugan PM. A bottom gravity current model for CO_2-enriched seawater. *Energy Conversion and Management* 1993; **34**:1065–1072.
6. Thorkildsen F, Alendal G. LES study of flow around a CO_2 droplet plume in the ocean. *Energy Conversion and Management* 1997; **38**:361–366.

7. Alendal G, Drange H. Two-phase, near-field modeling of purposefully released CO_2 in the ocean. *Journal of Geophysical Research* 2001; **106**:1085–1096.
8. Sato T, Sato K. Numerical prediction of the dilution process and its biological impacts in CO_2 ocean sequestration. *Journal of Marine Science and Technology* 2002; **6**:169–180.
9. Chen B, Song Y, Nishio M, Akai M. Large-eddy simulation on double-plume formation induced by CO_2 dissolution in the ocean. *Tellus B* 2004; **55**:723–730.
10. Sato T. Numerical simulation of biological impact caused by direct injection of carbon dioxide in the ocean. *Journal of Oceanography* 2004; **60**:807–816.
11. Chen B, Song Y, Nishio N, Someya S, Akai M. Modeling near-field dispersion from direct injection of carbon dioxide into the ocean. *Journal of Geophysical Research* 2005; **110**:C09S15.1–C09S15.13.
12. Masuda Y, Yamanaka Y, Sasai Y, Magi M, Ohsumi T. A numerical study with an eddy-resolving model to evaluate chronic impacts in CO_2 ocean sequestration. *International Journal of Greenhouse Gas Control* 2008; **2**:89–94.
13. Jeong S-M, Sato T, Chen B. Diffusion simulation of CO_2 discharged in mesoscale deep ocean by using moving-nesting grid technique. *International Journal of Offshore and Polar Engineering*, in press. [Correction made here after initial online publication.]
14. Sato T, Sato K, Jeong S-M. Numerical reconstruction of turbulent flow field in a small patch of open ocean. *Computers and Fluids* 2007; **36**:540–548.
15. Okubo A. Oceanic diffusion diagrams. *Deep Sea Research* 1971; **18**:789–802.
16. Ledwell JR, Watson AJ, Law CS. Mixing of a tracer in the pycnocline. *Journal of Geophysical Research* 1998; **103**:21499–21529.
17. Richardson LF. Atmospheric diffusion shown on a distance-neighbour graph. *Proceedings of the Royal Society A* 1926; **110**:709–737.
18. Munk WH, Anderson ER. Notes on a theory of the thermocline. *Journal of Marine Research* 1948; **7**:276–296.
19. Monaghan JJ. Simulating free surface flows with SPH. *Journal of Computational Physics* 1994; **110**:399–406.
20. Koshizuka S, Oka Y. Moving-particle semi-implicit method for fragmentation of incompressible fluid. *Nuclear Science and Engineering* 1996; **123**:421–434.
21. Kikkawa T, Kita J, Ishimatsu A. Comparison of the lethal effect of CO_2 and acidification on red sea bream during the early developmental stages. *Marine Pollution Bulletin* 2004; **48**:108–110.
22. Roy RN, Roy LN, Vogel KM, Porter-Moore C, Pearson T, Good CE, Millero FJ, Campbell DM. The dissociation constants of carbonic acid in seawater at salinities 5 to 45 and temperatures 0 to 45 deg C. *Marine Chemistry* 1993; **44**:249–267.
23. Kita J, Watanabe Y. Impact assessment of high-CO_2 environment on marine organisms. *Proceedings of the 8th International Conference on Greenhouse Gas Control Technology*, 2006. Available from: http://www.ieagreen.org.uk/ghgt8.html.